JBC RESEARCH ARTICLE

Iron regulatory protein 1 is required for the propagation of inflammation in inflammatory bowel disease

Received for publication, November 23, 2023, and in revised form, July 2, 2024 Published, Papers in Press, August 7, 2024,
https://doi.org/10.1016/j.jbc.2024.107639

Lulu Fahoum[1,‡], Shirly Moshe-Belisowski[1,‡], Kristina Zaydel[1], Niraj Ghatpande[1], Noga Guttmann-Raviv[1], Wenxin Zhang[2], Kuanyu Li[2], Wing-Hang Tong[3], Abraham Nyska[4], Matti Waterman[5], Ronni Weisshof[5], Avi Zuckerman[6], and Esther G. Meyron-Holtz[1,*]

From the [1]Laboratory of Molecular Nutrition, Department of Biotechnology and Food Engineering, Technion– Israel Institute of Technology, Haifa, Israel; [2]Jiangsu Key Laboratory of Molecular Medicine, Medical School of Nanjing University, Nanjing, China; [3]Molecular Medicine Program, Eunice Kennedy Shriver National Institute of Child Health and Human Development, Bethesda, Maryland, USA; [4]Department of Biotechnology and Food Engineering, Tel Aviv University and Consultant in Toxicologic Pathology, Tel Aviv, Israel; [5]Department of Biotechnology and Food Engineering, Rambam/Technion– Israel Institute of Technology, Haifa, Israel; [6]Department of Biotechnology and Food Engineering, Aviv Projects, Ness Ziona, Israel

Reviewed by members of the JBC Editorial Board. Edited by Donita C. Brady

Inflammatory bowel diseases (IBDs) are complex disorders. Iron accumulates in the inflamed tissue of IBD patients, yet neither a mechanism for the accumulation nor its implication on the course of inflammation is known. We hypothesized that the inflammation modifies iron homeostasis, affects tissue iron distribution, and that this in turn perpetuates the inflammation. This study analyzed human biopsies, animal models, and cellular systems to decipher the role of iron homeostasis in IBD. We found inflammation-mediated modifications of iron distribution, and iron-decoupled activation of the iron regulatory protein (IRP) 1. To understand the role of IRP1 in the course of this inflammation-associated iron pattern, a novel cellular coculture model was established, which replicated the iron-pattern observed *in vivo*, and supported involvement of nitric oxide in the activation of IRP1 and the typical iron pattern in inflammation. Importantly, deletion of IRP1 from an IBD mouse model completely abolished both, the misdistribution of iron and intestinal inflammation. These findings suggest that IRP1 plays a central role in the coordination of the inflammatory response in the intestinal mucosa and that it is a viable candidate for therapeutic intervention in IBD.

Inflammatory bowel diseases (IBDs) are long-term multifactorial inflammations of the gastrointestinal tract, with Crohn's disease (CD) and colitis being the two most common forms. Since the beginning of industrialization, global incidence has been rising and due to a lack of cure, global prevalence increases as well (1). Although the cellular and molecular events initiating and perpetuating the inflammation are not fully understood, it is clear that intestinal homeostasis is broadly disrupted, causing pathological inflammation that leads to tissue injury. Increased iron concentrations have been measured in the inflamed tissues of CD and colitis patients, when compared to tissue of healthy individuals and to patient samples collected from noninflamed regions (2), but neither the impact of nor the mechanism driving this phenomenon are known.

Iron is an essential nutrient, yet unbalanced iron levels lead to inflammation and tissue damage (3–5). Iron homeostasis is tightly regulated at the systemic and cellular level, primarily by the peptide hormone hepcidin (6) and by the two iron regulatory proteins (IRP1/2), respectively (7). Hepcidin acts by binding to the iron exporter ferroportin, where it sterically inhibits iron export and causes ferroportin degradation (8, 9). IRPs regulate numerous transcripts related to cellular iron import, storage and export, by binding with high affinity to RNA motifs known as iron-responsive elements (IREs). For example, binding of IRPs to the IRE in the 5′ UTR of the subunits (FtH and FtL) of the iron storage protein ferritin (10), inhibits their translation. Reducing the cytosolic ferritin levels will lead to less storage capacity and elevate iron availability. In contrast, IRP binding to the iron importer transferrin receptor 1 (TFR1) 3′ UTR IREs, stabilizes these transcripts, leading to increased iron import.

IRP1 is a bifunctional protein that primarily functioning as a cytosolic, iron-sulfur cluster-containing, aconitase (cAco). In iron-deficient conditions, it undergoes a conformational change and turns into an RNA (IRE)-binding apoprotein. Similar to IRP1, IRP2 binds to IREs in iron-deficient conditions, yet it is degraded in the presence of high iron. Both IRPs are also regulated by oxygen and reactive oxygen and nitrogen species. However, in contrast to their concerted iron regulation, their response to oxygen is opposing (11, 12). IRP2 is stable at physiologic oxygen and acts as an RNA-binding protein under these conditions. In contrast, the Fe-S cluster of cAco is relatively stable at low physiologic oxygen conditions, therefore IRP1 maintains its aconitase activity, even when iron levels are low (13–15).

Similar to the opposing response of the two IRPs to oxygen, they also respond differently to nitric oxide (NO). NO plays important roles in pathogen killing, as well as macrophage

‡ These authors both contributed most significantly to this work.
* For correspondence: Esther G. Meyron-Holtz, Meyron@technion.ac.il.

metabolic and epigenetic remodeling, and is elevated in inflammatory processes including IBD (16). The biological consequences of NO-mediated IRP1 activation *versus* IRP2 degradation on cellular iron, TfR1 and ferritin, were extensively studied in macrophages (17), yet their systemic role in specific inflammatory diseases remains unclear. We hypothesized that NO-mediated IRP1 activation drives the observed iron accumulation in the inflamed tissues of IBD patients, and thus perpetuates the inflammation.

The present work studied iron homeostasis in biopsies from CD patients, animal models for CD and colitis, and a cellular coculture model that mimics the interaction between intestinal epithelium and immune cells. IRP1 was found to be activated by inflammation. This inflammation-mediated regulation of IRP1 activity impaired intestinal iron homeostasis and arbitrated the propagation of inflammation in IBD. Most importantly, targeted deletion of IRP1 minimized the inflammation, flagging it as a novel target for the treatment of IBD.

Results

Intestinal inflammation triggers an iron-independent IRP1 activation and a cell-specific pattern of iron distribution

Tumor necrosis factor alpha-overexpressing mice ($Tnf^{\Delta ARE/+}$), which are a genetic mouse model for CD (18), and the chemical dextran sulphate sodium (DSS) model for colitis (19) were used to evaluate the effect of inflammation on iron homeostasis and IRP activity. $Tnf^{\Delta ARE/+}$ mice develop spontaneous inflammation in the terminal ileum (TI) early and rheumatoid arthritis later in life (18). Immunofluorescent stains (IFs) on intestinal sections of 12- to 14-week-old $Tnf^{\Delta ARE/+}$ mice were used to evaluate the level of ferritin, a sensitive indicator of cellular iron status (20). While ferritin accumulated in the immune cells (lamina propria [LP]), its levels were significantly reduced in intestinal epithelial cells (IECs) of the inflamed TI of $Tnf^{\Delta ARE/+}$ mice compared to WT controls (Figs. 1*A* and S1*A*). Similar trends were observed in sections from mice with DSS-induced colitis (Figs. 1*A* and S1*A*). To further analyze ferritin and other iron-related proteins, the TI of $Tnf^{\Delta ARE/+}$ mice was fractionated into IEC and LP fractions. In correlation with the IF data, a reduction in ferritin-iron and FtH and FtL subunits was detected in the IEC fraction from the inflamed TI of $Tnf^{\Delta ARE/+}$ mice compared to WT controls (Fig. S1*B*). Furthermore, a reduced FtH level was observed in the IEC fraction from mice with DSS-induced colitis (Fig. S1*B*). In addition, proteins known to respond to cellular iron levels were analyzed in each fraction separately. Consistent with the ferritin response to inflammatory conditions, IEC TFR1 levels were increased and LP TFR1 levels were reduced, when compared to the WT fractions (Fig. 1*B*). In addition, IRP2 levels were increased in the inflamed IECs and decreased in the inflamed LP (Fig. 1*C*). In contrast, IRP1-IRE–binding activity was significantly elevated in both fractions of the inflamed ileum compared to uninflamed ileum from WT mice, suggesting that the regulation of IRP1 activity is independent of the intracellular iron status (Fig. 1*D*). Taken together, intestinal inflammation triggered a unique pattern of iron distribution, involving iron accumulation in immune cells and iron deficiency in IECs.

Physical contact is required between macrophages and epithelial cells to mimic the activation of IRP1-IRE–binding activity in vitro

We searched for a suitable cell model to elucidate the forces driving the iron-independent activation of IRP1 and the intestinal inflammation-specific iron distribution pattern observed in mice. Several coculture models of epithelial cells (ECs) with immune cells separated by filter inserts have been successfully employed to reproduce various aspects of inflammation (21), yet none of these models could reproduce inflammation-specific iron patterns. We hypothesized that NO produced by macrophages diffuses and activates IRP1 in neighboring ECs, and that this activation mediates the inflammatory iron pattern. Thus, we tested cocultures with direct cell-to-cell contact between ECs and macrophages. To enable differentiation between EC- and macrophage-derived proteins, a direct interspecies coculture model was developed with human epithelial enterocyte-like Caco2 cells and either murine primary bone marrow–derived macrophages (BMDMs) or the murine macrophage–like cell line Raw 264.7 (22). Lipopolysaccharide (LPS)-induced inflammation was validated by the activation of critical markers of signaling pathways involved in inflammation, including MAP kinase pathways and NFkB-p65 (Fig. S2*A*) (23, 24). In addition, downstream proinflammatory cytokines—including *IL8* and *ICAM1* in ECs (Fig. S2*B*) and *Tnfα*, *Icam1*, *Il1b*, and *Il6* in macrophages (Fig. S2*C*)—were all activated in both cocultures and the time-course of the LPS-triggered inflammatory response was nearly identical to that reported for *in vivo* and *in vitro* models of LPS-induced inflammation (25).

The LPS-triggered response was identified in both macrophage monocultures and macrophage EC cocultures, but not in EC monocultures (Fig. S3*A*), suggesting the need for macrophages to elicit the epithelial inflammatory response. Indeed, application of the NO donor S-nitro-N-acetyl-D, L-penicillamine (SNAP) elicited an inflammatory response in EC monocultures (Fig. S3*B*). Further, in SNAP-treated EC monocultures, intracellular iron was reduced and extracellular iron increased (Fig. S3*C*), supporting the notion that NO generated in macrophages contributes to the inflammatory iron pattern in ECs.

In parallel, the RNA-binding activity of macrophage IRP1 was significantly increased after LPS stimulation (Fig. 2*A* lane 3 and 4), similar to the observation in the $Tnf^{\Delta ARE/+}$ mice (Fig. 1*D*). Yet, epithelial IRP1 could not be evaluated in a gel shift assay, as it migrated together with macrophage IRP2. Therefore, IRP1 aconitase activity was evaluated using the in-gel aconitase-assay, as decreased cAco activity correlates with increased IRP1 RNA-binding-activity. Gel conditions were optimized to enable differentiation between human *versus* mouse cAco activity (Figure 2*B* lane 1 and 4). A decrease in cAco activity was observed in response to LPS treatment in both cell types, which is consistent with an increase in the RNA-binding activity of IRP1. Moreover, LPS treatment led to

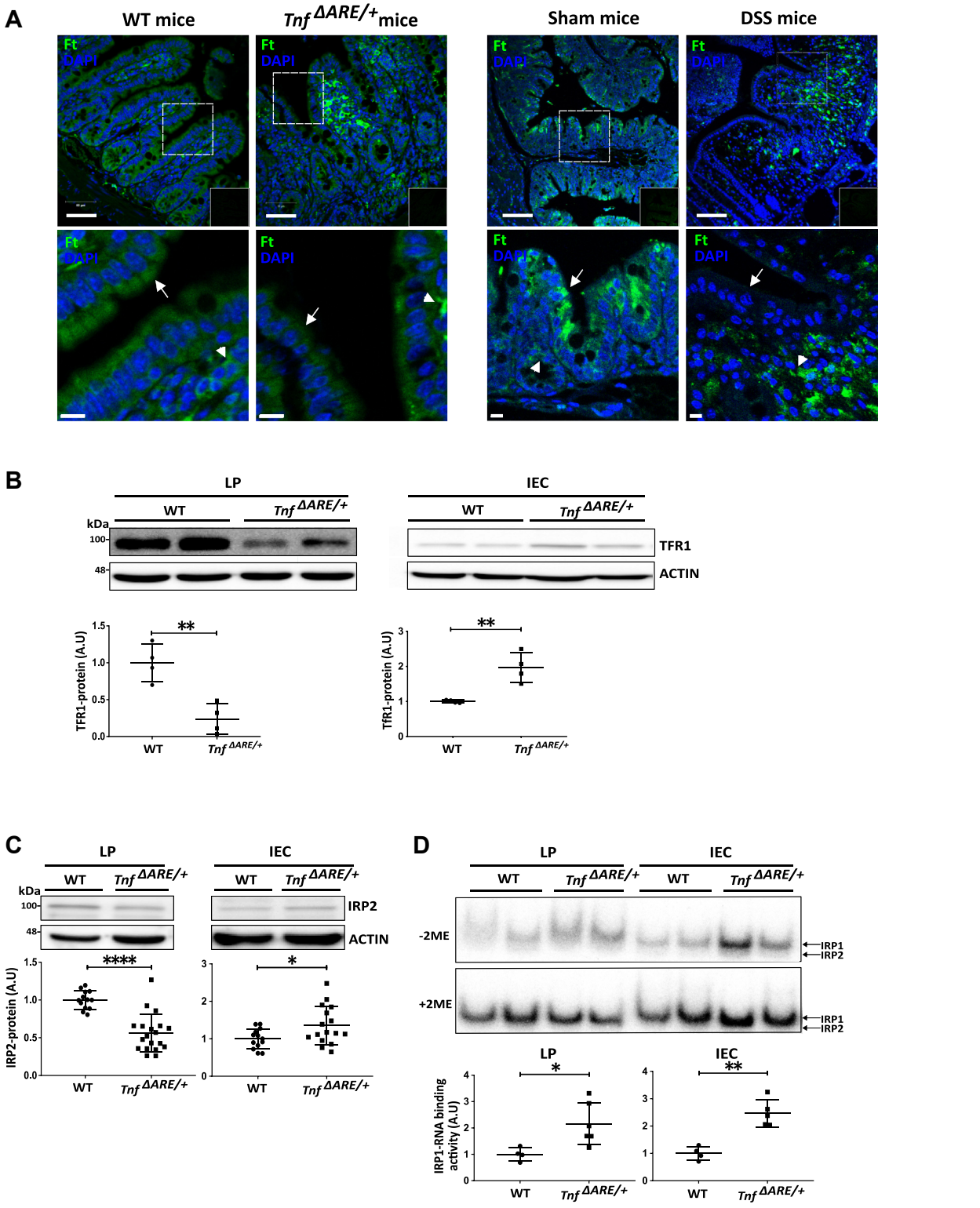

Figure 1. Inflammation drives a cell-specific pattern of iron distribution. *A*, sections from terminal ileum (TI) of 12- to 14-week-old WT and *Tnf* $^{\Delta ARE/+}$ mice (n = 3 each), as well as C57BL/6 mice treated for 7 days with drinking water supplemented with 4% dextran sulfate sodium (DSS), were immunostained for ferritin (*green*). Representative images show decreased ferritin levels in the inflamed intestinal epithelial cells (IEC) (*arrows*). Lamina propria (LP) cells show increased ferritin levels (*arrow heads*) in both inflammation models. Scale bars in the *lower* magnification represent 50 μm and 10 μm in the higher magnification. Negative controls of secondary antibody only are inserted in the *lower right corner* of the lower magnification image. *B–D*, TI was harvested from 12- to 14-week-old WT and *Tnf* $^{\Delta ARE/+}$ mice. IEC- and LP-enriched fractions were isolated and lysates further analyzed. *B*, representative immunoblot for transferrin receptor-1 (TFR1) (mean ± SD (n = 4)). *C*, representative immunoblot for IRP2 (mean ± SD (n > 16)). *D*, representative radiograph of electromobility shift assay (EMSA) and quantification of IRP1-RNA–binding activity. Addition of 2-mercaptoethanol (2-ME) to the lysate removes all Fe-S clusters from cAco/IRP1 and thus shows total IRP1-RNA–binding capacity. Values were normalized to +2-ME (mean ± SD (n > 4)). Quantifications (*B–D*) were done, using Image J (https://imagej.net/ij/) and immunoblots were normalized to actin (*B–C*). IRP, iron regulatory protein.

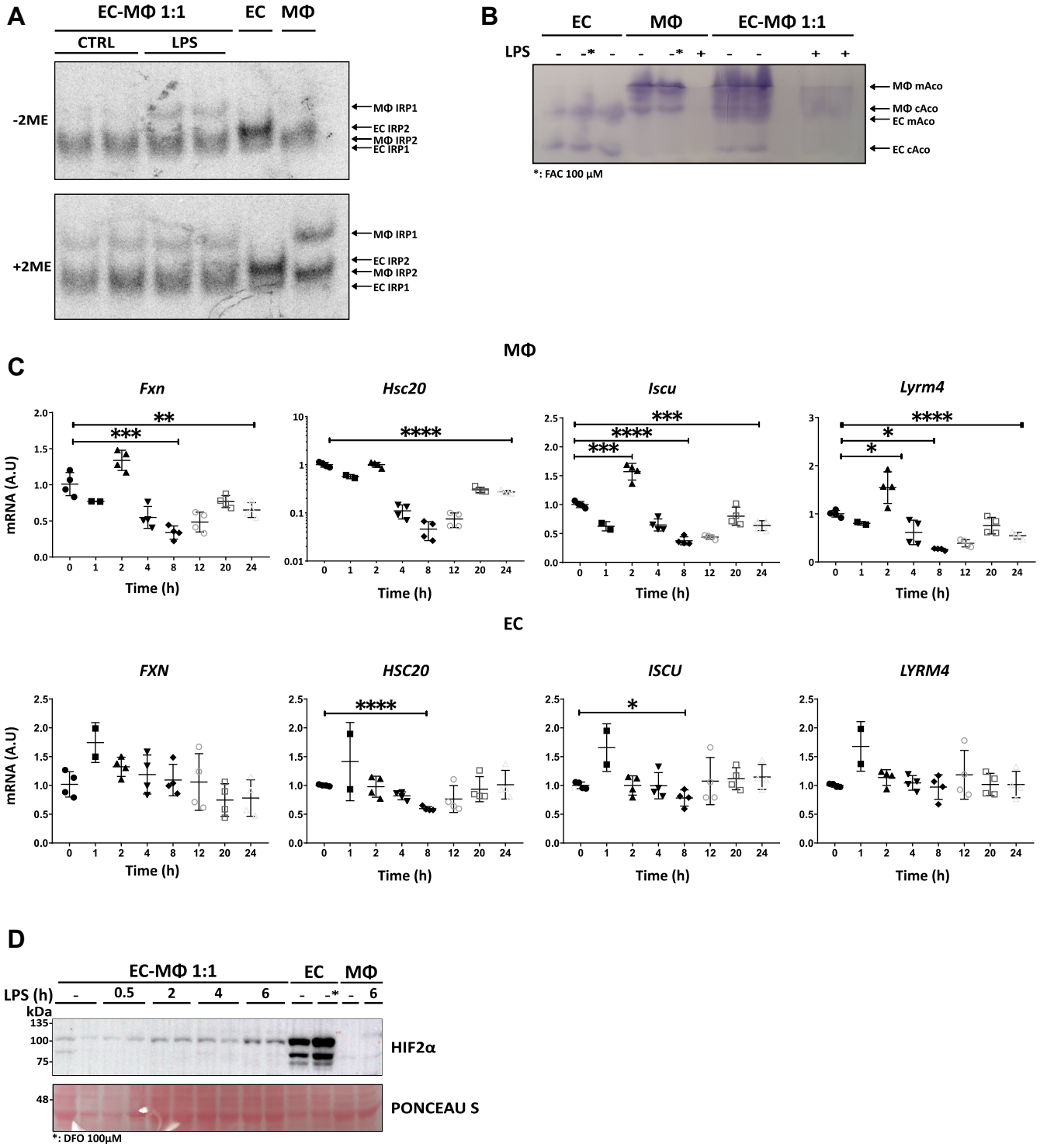

Figure 2. An interspecies coculture model mimics the inflammation-associated activation of IRP1. Cocultures of epithelial cells (ECs) and macrophages (MΦ) were treated with 200 ng/ml lipopolysaccharide (LPS) for 24 h. Cells were harvested and lysed. *A*, lysates were subjected to electromobility shift assay (EMSA) for assessment of IRP-RNA–binding activity (n = 4). A representative radiograph is shown. *B*, lysates were subjected to in-gel aconitase assay (n = 4). A representative gel is shown. *C*, expression levels of mRNA of key proteins associated with iron-sulfur cluster biogenesis were measured by RT-qPCR following induction of inflammation with LPS. *D*, representative immunoblot of cytosolic fraction (n = 4). * 100 µM desferrioxamine (DFO) for 24 h. In cocultures, EC were always Caco2 cells. MΦs were as follows: Raw264.7 in A-B, and bone marrow–derived macrophages (BMDMs) in *C–D*. IRP, iron regulatory protein; RT-qPCR, quantitative RT-PCR.

a significant decrease in mitochondrial aconitase activity in both cell types, suggesting a metabolic shift to glycolysis, as previously reported (26, 27). Taken together, the direct interspecies coculture model developed here, demonstrated activation of a broad range of inflammatory signaling pathways upon LPS-induced inflammation. Most importantly, the cell-

model replicated the increased IRP1 mRNA-binding activity as seen *in vivo* (Fig. 1*D*).

We reasoned that increased IRP1 RNA-binding activity may be due to impaired Fe-S cluster assembly. This was based on the fact that the cysteine-desulfurase of the core iron-sulfur cluster assembly complex Nfs1 and the iron-sulfur cluster assembly enzyme IscU mRNA and protein levels were reported to be low in BMDM in response to inflammation (28). Thus, several genes involved in Fe-S cluster assembly were evaluated. In macrophages, the transcription levels of all four tested iron-sulfur cluster biogenesis proteins were significantly decreased, in agreement with the decrease in aconitase activities in mitochondrial aconitase and cAco. However, in ECs, transcripts of iron-sulfur cluster biogenesis proteins did not change (Fig. 2*C*). In IBD, the epithelial transcription regulator hypoxia inducible factor (HIF)2α is increased (29), and given that HIF2α is a key regulator of iron transport through ECs (30), cytosolic, and nuclear levels of HIF2α, were tested. We found that HIF2α was significantly increased in ECs, beginning 4 h after LPS stimulation (Fig. 2*D*). In line with this, 4 h after LPS stimulation, levels of both the apical iron importer divalent metal transporter 1 and the basolateral iron exporter ferroportin (FPN) gradually increased (Fig. S4), likely promoting iron flux from the intestinal lumen, through the ECs and into the blood. This can explain the observed epithelial iron deficiency and consequential increase in IRP1 RNA-binding activity. In summary, increased NO production, decreased iron-sulfur cluster assembly proteins in macrophages and increased HIF2α in ECs support the inflammation-induced activation of IRP1-IRE–binding activity in both cell types.

The epithelial-macrophage coculture mimics the cell-specific pattern of iron distribution

To test the effect of inflammation on iron homeostasis, changes in ferritin-iron content were analyzed upon LPS stimulation of cocultures. Epithelial ferritin iron was reduced and macrophage ferritin iron was elevated 24 h after LPS stimulation (Fig. 3*A*). Similar results were obtained when ECs and macrophages were preloaded with ^{55}Fe (Fig. S5*A*). In addition, a strong increase in ferritin protein, especially of the FtH subunit, was detected in the macrophages of the cocultures (Fig. 3*B*), consistent with the observations in macrophage monocultures (31). We thought that the increase of ferritin in macrophages, despite the activation of macrophage IRP1, could be due to an inflammation-mediated decrease in ferritin degradation. Pulse-chase analysis of cocultures that were metabolically labeled with ^{35}S just before stimulation with LPS showed that macrophage ferritin subunit degradation was slower in LPS-treated cocultures (Fig. 3*C* lane 11) compared to untreated controls (Fig. 3*C* lane 10). A decrease in ferritin degradation was further suggested by a decrease in transcript levels of the ferritinophagy-mediating *Ncoa4* in inflamed BMDM (Fig. 3*D*). After 24 h of LPS stimulation, macrophage ferritin migrated slightly faster in native gels, than its nontreated counterpart (Figs. 3*A*, and S5*A*), suggesting a shift in subunit composition toward H-rich heteropolymers. The shift in subunit composition can easily be analyzed on native gels (Fig. S5*B*). Indeed, the transcript levels of *Fth* were markedly increased after LPS stimulation, whereas transcript levels of *Ftl* remained relatively unchanged (Fig. S5*C*). A similar increase in FtH levels was reported in monocytes exposed to inflammatory conditions (32). In agreement, the FtH:FtL protein ratio shifted from approximately 1:1 to approximately 3:1 after LPS stimulation (Fig. S5*D*). In contrast, LPS stimulation of ECs led only to a slight increase in *Fth* transcript levels, alongside a significant increase in *Ftl* transcript levels (Fig. S5*C*). Nevertheless, epithelial ferritin protein concentration remained below detectable levels in immunoblots; only epithelial ferritin-iron could be detected, and this was decreased after 24 h of LPS stimulation (Fig. 3*A*). In summary, the intricate processes of ferritin synthesis and degradation during inflammation align with the observed increase in macrophage ferritin and ferritin iron, as well as the decrease in epithelial ferritin iron. These findings are consistent with the observations in the inflamed lesions of $Tnf^{\Delta ARE/+}$ mice (Fig. 1*A*).

To further validate the observed inflammatory iron pattern in the epithelial-macrophage coculture, changes in mRNA levels of the iron importer TFR1 were evaluated following LPS induction (Fig. 3*E*). We found that *Tfr1* mRNA and protein levels decreased in the macrophages and increased in the ECs 24 h after LPS exposure, consistent with the iron accumulation in the macrophages and the iron decrease in the IECs of the $Tnf^{\Delta ARE/+}$ mice. The *Tfr1* mRNA decrease in macrophages was preceded by an increase in *Tfr1* transcripts, identified 2 h after LPS stimulation, suggesting an early inflammation-mediated increase in iron import that contributes to iron accumulation in the macrophages (Fig. 3, *E* and *F*). Taken together, in ECs, the decrease in ferritin and increase in TFR1 are in line with the activation of IRP1. However, in the macrophages, the IRP1 activation was decoupled from high cellular iron status, and ferritin and TFR1 regulation were dominated by the iron-loaded phenotype.

IRP1 activity contributes to the propagation of inflammation

Since IRP1-RNA–binding activity was increased in inflamed macrophages, regardless of their iron-loaded phenotype (Figs. 1–3), we hypothesized that this activation may play a role in the course of the inflammation. Thus, the effect of IRP1 knockout in macrophages on inflammatory markers and iron pattern was assessed. The classical inflammatory response of cocultures involving $Irp1^{-/-}$ macrophages was reminiscent of the cocultures with WT macrophages in all inflammatory parameters tested, including the levels of secreted epithelial cytokine IL-8 and transcript levels of the macrophage inflammation markers *Tnfα, Icam1,* and *Il6* (Fig. S6, *A* and *B*). In parallel, NO levels in the medium of both cocultures (EC with WT or $Irp1^{-/-}$ macrophages) were similarly increased in response to LPS stimulation (Fig. S6*C*). Furthermore, FtH was significantly increased in macrophages of both genotypes in inflamed cocultures (Fig. 4*A*), while aconitase activities were

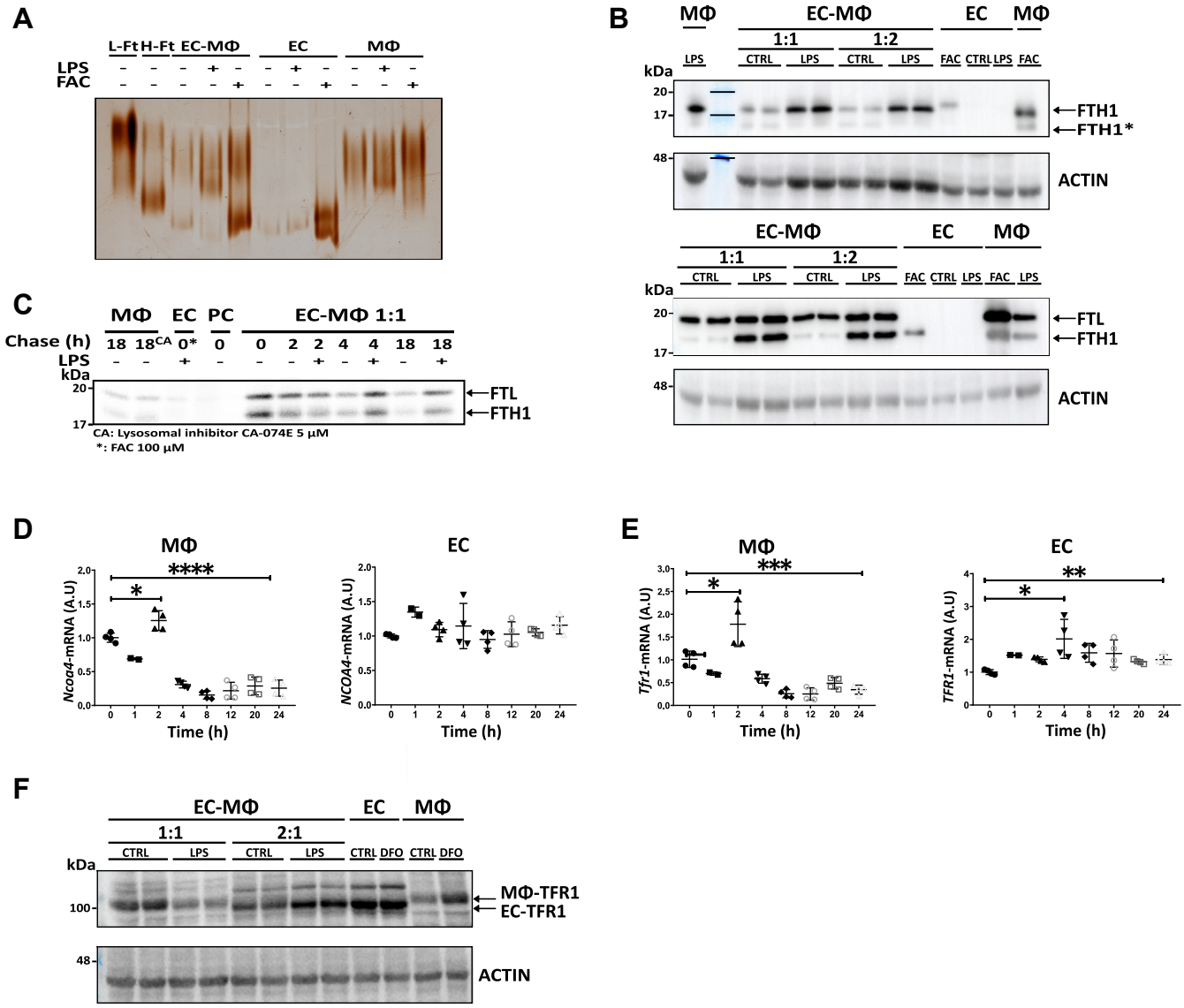

Figure 3. Iron-regulated proteins sense and respond to reduced epithelial and increased macrophage iron levels. Cocultures of epithelial cells (ECs) and macrophages (MΦ) were treated with 200 ng/ml lipopolysaccharide (LPS), ferric ammonium citrate (FAC), or desferrioxamine (DFO) for 24 h or as indicated. *A*, lysates (40 μg/lane for MΦ and 60 μg/lane for EC and cocultures) were analyzed on native gels, followed by Perls-DAB staining to detect ferritin-iron. (n = 2) *B*, representative immunoblot for the ferritin H-subunit (FTH1) and ferritin L-subunit (FTL). EC ferritin was not detected (except in FAC-treated ECs), thus the bands are MΦ ferritin only. Anti-FtL antibody detects both subunits (FTH1 is the lower band just above the 17kD Mw-marker) n = 4. *C*, metabolic labeling (^{35}S) pulse-chase experiment of LPS-stimulated EC-MΦ (BMDM) cocultures, followed by ferritin immunoprecipitation (IP) (n = 2). *D*, RNA expression levels of *Ncoa4* were measured in cocultures by RT-qPCR (n = 4). *E*, transferrin receptor-1 (*Tfr1*) RNA expression levels were measured by RT-qPCR (n = 4). *F*, a representative immunoblot for TFR1 (n = 12). In cocultures, EC were always Caco2 cells. MΦs were as follows: BMDM in A-E, and Raw264.7 in F. BMDM, bone marrow–derived macrophage; DAB, 3,3′-diaminutesobenzidine; FAC, ferric ammonium citrate.

significantly decreased in both cocultures (Fig. 4*B*), indicating that deletion of IRP1 in the macrophages alone is not responsible for the inflammatory changes in iron homeostasis.

As ECs have been shown to play a critical role in the pathophysiology of IBD (33), and epithelial iron deficiency has been associated with an inflammatory response (34), the effect of epithelial IRP1 activation on the inflammation was assessed. Activation of IRP1 was previously achieved by a stable aminoxyl radical Tempol (35). LPS stimulation of cocultures with Tempol-pretreated ECs, elicited a more significant inflammatory response in the ECs compared to ECs in cocultures without Tempol pretreatment (Fig. 4*C*). Without LPS stimulation, Tempol treatment alone did not elicit a significant inflammatory response in the cocultures. Yet, a trend of increased murine *Tnfα, Icam1,* and human *ICAM1* was observed, when IRP1 was activated (Fig. S6*D*). These results suggested that epithelial IRP1 contributes to the course of the inflammation.

To test this, we introduced a targeted deletion of *Irp1* into the *Tnf* $^{\Delta ARE/+}$ mice. To easily monitor iron levels in the tissue sections, mice were previously subjected to iron overload. As expected, a significant increase in LP ferric iron levels was observed in *Tnf* $^{\Delta ARE/+}$ mice compared to WT mice. In contrast, *Tnf* $^{\Delta ARE/+}$, *Irp1*$^{-/-}$ mice showed no increase in LP

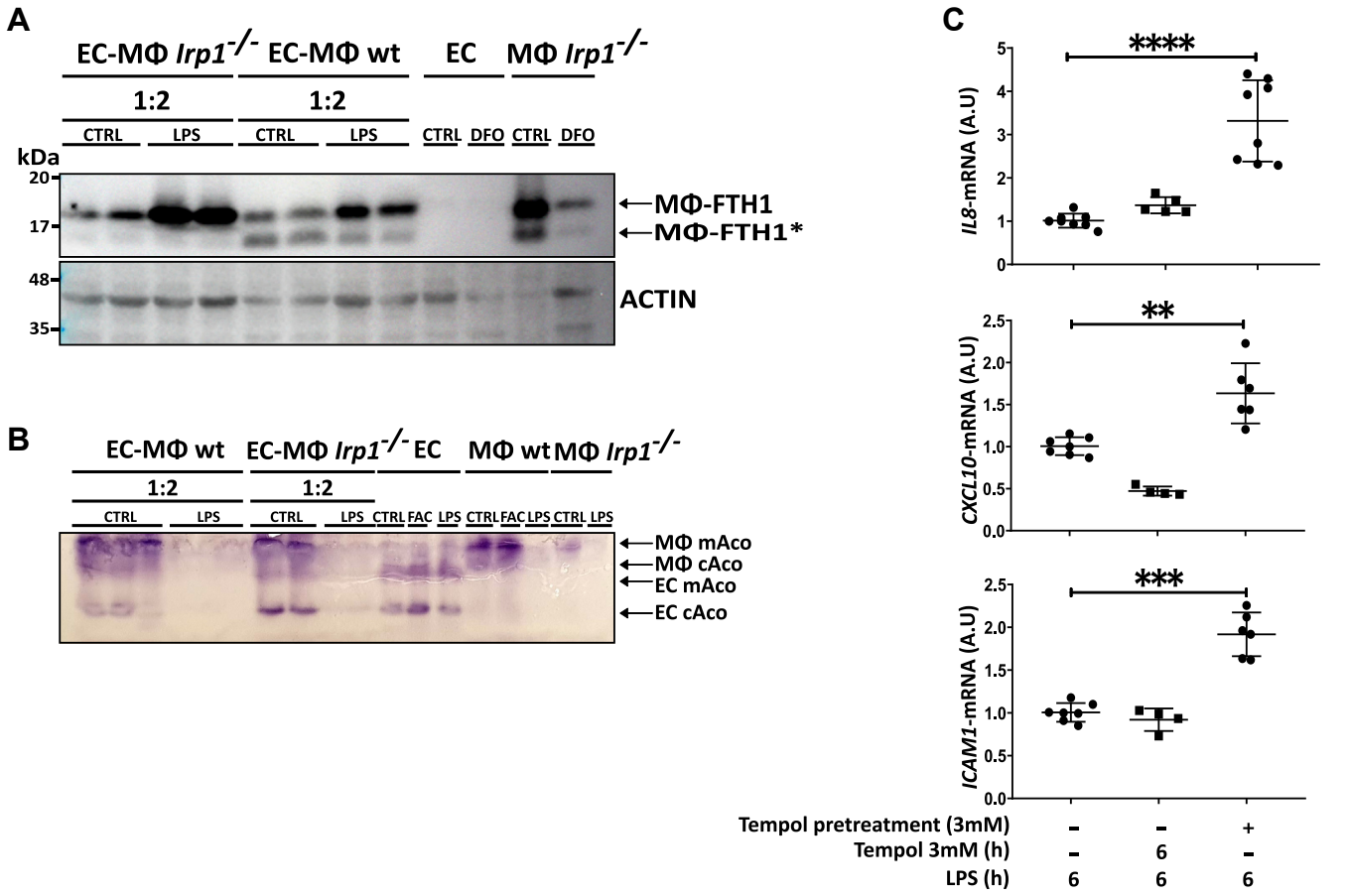

Figure 4. Macrophage and epithelial IRP1-IRE–binding plays different roles in intestinal inflammation. *A* and *B*, cocultures of epithelial cells (ECs) with WT-bone marrow–derived macrophages (BMDMs) or with BMDM with targeted deletion of IRP1 (MΦ *Irp1*$^{-/-}$) were treated with 200 ng/ml lipopolysaccharide (LPS) and ECs and BMDMs were treated with ferric ammonium citrate (FAC), or desferrioxamine (DFO) for 24 h, as indicated. *A*, a representative immunoblot for FtH is shown (*FtH-degradation product) (n = 8). *B*, a representative gel of an in-gel aconitase assay is shown (n = 4). *C*, ECs (Caco2) were pretreated with 3 mM Tempol for 16 h, washed, and then cocultured with MΦs (Raw 264.7). After MΦs adhered, LPS and/or Tempol was added for 6 h. RNA expression levels were measured by RT-qPCR (n = 6). IRE, iron-responsive element; IRP, iron regulatory protein.

iron levels similar to the noninflamed LP in WT mice (Fig. 5*A*). Severity of inflammation was evaluated in mice without iron overload. *Tnf* $^{\Delta ARE/+}$, *Irp1*$^{-/-}$ mice showed no histological signs of inflammation (Figs. 5, *B*, *C* and S7*A*) and a significantly reduced proinflammatory response, as indicated by reduced *Tnfα* and *Icam1* levels (Fig. 5*D*). These results indicated that activation of IRP1-RNA–binding activity is required for the propagation of TI inflammation in *Tnf* $^{\Delta ARE/+}$ mice.

Modified iron homeostasis is observed in the inflamed lesions of CD patients

Finally, to determine whether the inflammatory iron homeostasis observed in the mouse models as well as in our coculture models mimics the impaired iron homeostasis in CD patients, sections of intestinal biopsies from CD patients were labeled for ferritin. Indeed, ferritin levels proved to be significantly lower in IECs of inflamed than noninflamed areas from the same patients (Figs. 6*A* and S7*B*). This suggested that also in IBD patients, iron homeostasis is mediated by inflammatory IRP1 activation. Thus, inhibiting IRP1-RNA–binding activity in inflamed intestinal lesions may result in a reduction in intestinal inflammation and serve as a novel approach to treat IBD.

Discussion

Both, genetic and environmental influences play pivotal roles in the onset of IBD. However, the precise interplay through which these factors influence the composition of the gut microbiota, compromise the integrity of the intestinal barrier, recruit the immune system, and trigger the inflammatory process, remains elusive. Nonetheless, it has been established that local immune cells undergo activation, leading to the release of NO, alongside an array of other inflammatory molecules and cytokines in the affected region during the initial stages (36). Here, we demonstrated an inflammation-mediated activation of IRP1 in both, IEC and LP, driven by NO and decoupled from the cellular iron level in macrophages.

A pathological iron distribution was observed in human biopsies from CD patients, and in mouse models for CD and colitis and was replicable in cellular cocultures. It is characterized by decreased iron stores in IECs and increased iron stores in LP macrophages. Inflammation is a response to

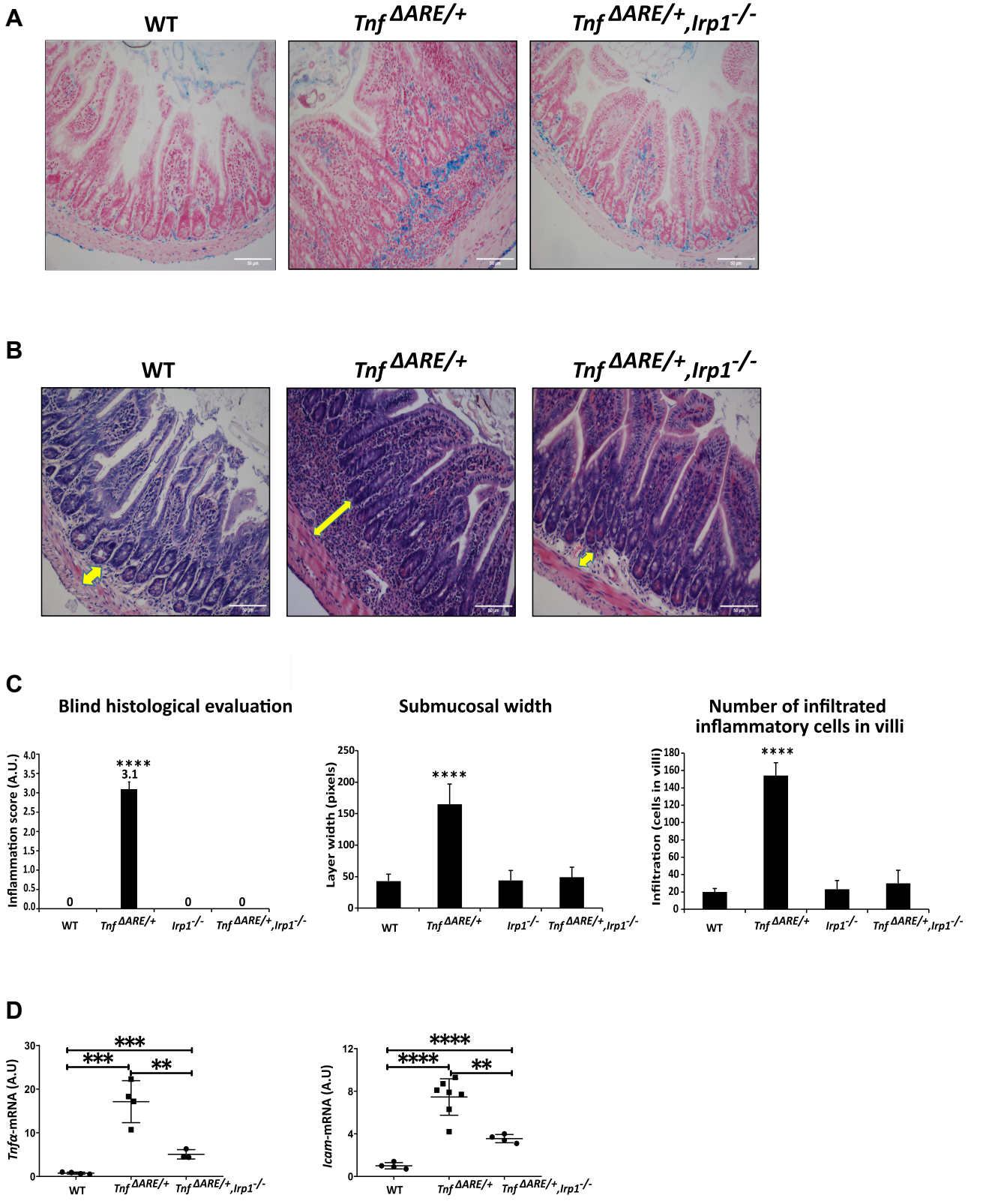

Figure 5. Deletion of IRP1 restores iron homeostasis and inhibits the inflammatory process in *Tnf* $^{\Delta ARE/+}$ mice. *Tnf* $^{\Delta ARE/+}$ mice were crossed with *Irp1* $^{-/-}$ mice until *Tnf* $^{\Delta ARE/+}$, *and Irp1* $^{-/-}$ mice were created. Sections from terminal ileum (TI) of 12- to 14-week-old mice from indicated genotypes were prepared. *A*, representative images of Perls-stained TI sections of iron-overloaded mice, illustrating iron distribution in *Tnf* $^{\Delta ARE/+}$, *Irp1* $^{-/-}$ mice is similar to WT and not to *Tnf* $^{\Delta ARE/+}$ mice. *B*, representative H&E-stained TI sections of noniron-overloaded mice, illustrating normal histology in *Tnf* $^{\Delta ARE/+}$, *Irp1* $^{-/-}$ mice, compared to *Tnf* $^{\Delta ARE/+}$ mice. The *arrows* highlight the width of the submucosal layer. *C*, blind histological evaluations of TI sections from 12- to 14-week-old WT, *Irp1* $^{-/-}$, *Tnf* $^{\Delta ARE/}$+, and *Tnf* $^{\Delta ARE/+}$, *Irp1* $^{-/-}$ mice (n = 6). *D*, RNA expression levels of select proinflammatory cytokines were measured by RT-qPCR (n = 4–7) in RNA from TI of 12-14-week-old WT, *Irp1* $^{-/-}$, *Tnf* $^{\Delta ARE/+}$, and *Tnf* $^{\Delta ARE/+}$, *Irp1* $^{-/-}$ mice. IRP, iron regulatory protein; RT-qPCR, quantitative RT-PCR.

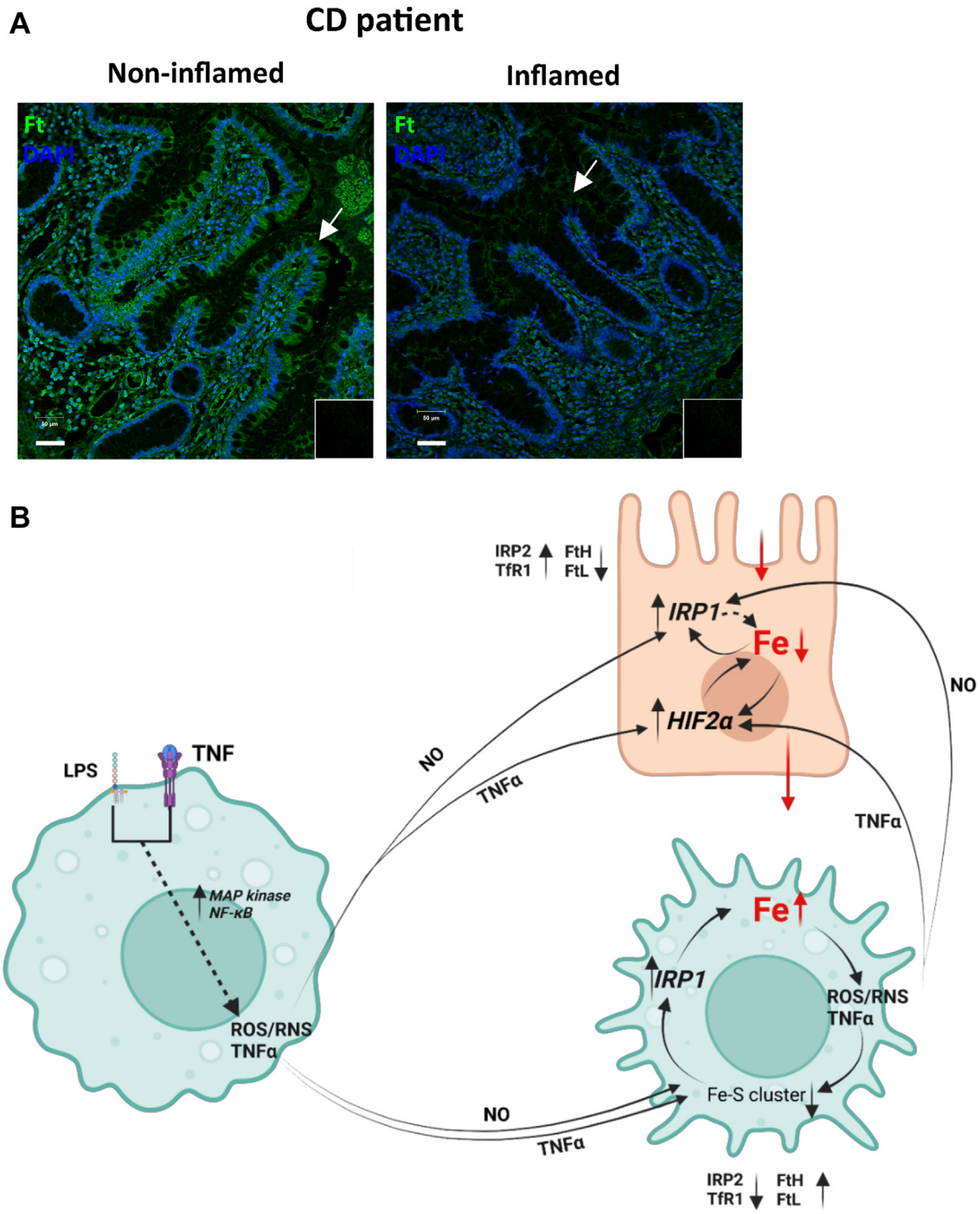

Figure 6. Modified iron homeostasis is observed in the inflamed lesions of Crohn's disease patients. *A*, sections from noninflamed and inflamed intestinal areas of Crohn's disease patients (n = 8) were immuno-stained for ferritin (*green*). Representative images show that the inflamed epithelial cells (IECs) (*arrows*) have decreased ferritin levels. Scale bars represent 50 μm. Negative controls of secondary antibody only are inserted in the *lower right corner* of the image. *B*, a schematic presentation of the involvement of IRP1 in the self-perpetuating inflammatory process. Macrophages activated to a proinflammatory response secrete nitric oxide (NO) and proinflammatory cytokines, such as TNFα to their immediate environment, enabling them to reach neighboring cells, including epithelial cells. In epithelial cells, TNFα activates the hypoxia-inducible factor HIF2α, which mediates increased iron flux from the intestinal lumen to the lamina propria, while NO activates IRP1, which inhibits ferritin translation and thus inhibits ferritin storage, which further increases iron flux. In macrophages, NO activates IRP1 and thereby maintains a certain level of increased iron influx that continues to promote iron overload, which supports the proinflammatory polarization of the macrophage. The inflammation-mediated reduction in iron-sulfur cluster assembly in macrophages and increase in HIF2α in epithelial cells continue to support the activity of IRP1 and the iron flux from epithelial cells to macrophages, which maintains the inflammatory iron pattern and perpetuates inflammation. HIF, hypoxia inducible factor; IRP, iron regulatory protein.

structural or functional insults, and an integral part of animal physiology, particularly as a means to correct homeostatic instability (37). The iron shift induced a homeostatic instability that eventually perpetuated an inflammatory process, as both increased and decreased iron levels were shown to mediate inflammation (3–5).

IRP1 regulates propagation of inflammation

The data suggest that the inflammation-associated iron pattern was driven by the activation of IRP1. Similarly, in a model of nonalcoholic fatty liver disease, elevated IRP1-RNA–binding activity was found despite high iron levels in rat livers (38), demonstrating activation of IRP1 in an inflammatory context, decoupled from iron status. In IBD, increased reactive oxygen/nitrogen species release from activated macrophages and reduced Fe-S cluster assembly can explain the IRP1 activation (39). The presented results demonstrated iron-decoupled activation of IRP1 in macrophages, and suggested that this activation signals a pseudo-iron deficiency, contributing to further iron influx (6).

In ECs, HIF2α was activated (Fig. 2*D*), in line with reports of NFkB-p65 activation, eliciting the activation of HIF2α (40). HIF2α activation is possibly further supported by NO-mediated iron efflux (41), which leads to prolyl-hydroxylase deactivation and HIF2α stabilization (42). HIF2α activation induces increased iron flux, which includes iron import through the apical membrane and iron export from the basolateral membrane, securing the repletion of body iron levels in iron deficiency (30). This increased iron flux may further contribute to the reduced iron levels in the ECs and the ensuing activation of IRP1. In addition, drug-induced activation of IRP1 in ECs increased the production of proinflammatory cytokines by these cells (Fig. 4*D*). Thus, the activation of IRP1-RNA–binding activity plays a role in the establishment of an inflammatory iron homeostasis that supports the exacerbation of the inflammatory process, as summarized in Figure 6*B*. This model is supported by our key finding that deletion of IRP1 abolished inflammation in *Tnf*α-overexpressing mice (Fig. 5, *A*–*D*). In line with this, in a model of uropathogenic *Escherichia coli*–induced orchitis, global knockout of IRP1 caused less testicular damage and a reduced immune response (43). This observation further strengthens the role of IRP1 in exacerbating inflammation.

Direct interference with intestinal iron homeostasis, by administering a low-iron diet, reduced inflammation in $Tnf^{\Delta ARE/+}$ mice (44). Interestingly, systemic iron chelation did not have a similar effect (44), supporting a role for local iron homeostasis in the course of the inflammation. Further, decreased iron content in the intestinal lumen elicited a lactobacillus-mediated reduction of iron uptake by decreasing HIF2α activity (45). Overall, this suggests a connection between the microbial composition or activity with epithelial iron homeostasis and thus also epithelial IRP1 activity. In addition, local regulation of iron homeostasis was also demonstrated to play an important role in the pathophysiology of IBD. For example, local production of hepcidin, (generally regarded as a systemic iron regulator) by conventional dendritic cells in the colon, regulates luminal iron content and supports colonic tissue repair (46). Inflammation-driven regulation of iron homeostasis may thus be a factor that plays an active role in the series of events that contribute to the course of inflammation.

The presented data, demonstrating opposing inflammatory regulation of iron homeostasis in macrophages *versus* ECs in the same tissue, complicated studying mechanisms that drive iron redistribution. We therefore looked for a cellular coculture system featuring the same inflammation-associated iron distribution pattern. Many of the published coculture setups mimicked well-established inflammatory parameters, however did not replicate the inflammatory iron pattern. This work showed that the inflammatory iron homeostasis was only established when ECs and macrophages were in direct contact. This cell-to-cell contact enabled us to replicate the iron and ferritin distribution that was observed in the $Tnf^{\Delta ARE/+}$ and DSS mouse models and IBD patients. Similar interspecies cocultures of Caco2 cells and Raw264.7 cells were successfully applied to analyze inflammatory pathways (22). Also, human grafts of fetal intestine in severe combined immunodeficiency disease mice were used to study fistulae in IBD (47), supporting the functionality of human-mouse interspecies systems. Interspecies cocultures have many advantages, especially in our study, they enabled us to differentially analyze iron-related proteins from epithelial *versus* macrophage origin. Using this model, we found that in response to the induction of inflammation, TFR1 was regulated by the iron status of the specific cell types (elevated in ECs and decreased in macrophages), as seen in the $Tnf^{\Delta ARE/+}$ animal model. Cocultures of WT ECs with BMDM from $Irp1^{-/-}$ mice did not result in reduced inflammation following LPS stimulation. In contrast, activation of IRP1 in the ECs further increased the inflammatory response, suggesting that the IRP1 activation in the ECs may be the driving force of the exacerbation of the inflammation by IRP1. The interspecies coculture also enabled analysis of inflammation-mediated changes in ferritin. In the macrophages, significant increases in both ferritin protein and ferritin-iron, as well as a shift in the ferritin composition toward FtH-rich complexes were measured in response to inflammation. Considering that NCOA4 binds specifically to FtH, and not to FtL (48), the change in subunit composition may have important implications on ferritin trafficking. In light of the recent findings that ferritin–NCOA4 complexes generate liquid-phase condensates (49, 50), and taking into account, that ferritin is an abundant and large cytosolic protein, the inflammation-specific ferritin subunit ratio may alter the physicochemical properties and the dynamics of the cytosol in inflammation.

In the physiologic, noninflamed state, IRP2 plays a dominant role in iron regulation, and deletion of IRP1 plays only a transient role (12, 14, 51, 52). In addition, reduction of IRP1 protein levels and activity in the noninflammatory setting of superoxide dismutase 1 KO mice was previously reported to have no effect on iron homeostasis (53). Yet, in patients with genetic hemochromatosis, dysregulation of IRP1 and IRP2 has been observed and was attributed to the release of NO produced in activated macrophages (17). Our results suggest, that IRP1 activation by inflammatory signals, contributes to the exacerbation of inflammation.

Conclusions

Taken together, the presented findings demonstrated that an inflammation-induced shift in the regulation of cellular iron homeostasis is mediated by the activation of IRP1, and that

this shift plays an active role in the propagation of inflammation in IBD. Further, correction of iron homeostasis by interfering with IRP1 activity halted the self-perpetuation of inflammation. Thus, unlike conventional therapeutic approaches which focus on modulating the immune system, our findings may pave the way for new therapeutic interventions for IBD by targeting IRP1.

Experimental procedures

Mice

Housing

Mice were housed in specific pathogen-free animal facilities at the animal facility of the Technion, Haifa, Israel, and studies were carried out in accordance with the recommendations in the Guide for the Care and Use of Laboratory Animals of the preclinical research authority at the Technion. The protocols were approved by the Technion Animal Ethics Committee (IL-135-09-19). For the DSS model, the protocols were approved by the Animal Investigation Ethics Committee of the affiliated Drum Tower Hospital of Nanjing University Medical School and were performed according to the Guidelines for the Care and Use of Laboratory Animals published by the National Institutes of Health.

Mice with genetic modifications

IRP1 KO (*Irp1*$^{-/-}$) mice on C57BL/6 background (*Irp1*$^{-/-}$) were a generous gift from Dr Tracey Rouault (Molecular Medicine Program, National Institute of Child Health and Human Development, NIH). *Tnf* $^{\Delta ARE/+}$ mice on C57BL/6 background (*Tnf* $^{\Delta ARE/+}$) were received initially from Prof. F. Cominelli at Case Western University and later from Prof. George Kollias, BSRC Alexander Fleming Athens University Medical School. *Tnf* $^{\Delta ARE/+}$ mice with targeted deletion of *Irp1* were generated by crossing *Tnf* $^{\Delta ARE/+}$ mice with *Irp1*$^{-/-}$ mice. WT littermates from breeders of *Tnf* $^{\Delta ARE/+}$ with WT mice and age- and sex-matched *Irp1*$^{-/-}$ mice were used as controls in the experiments described here.

Systemic iron overload of mice

Fe-dextran (Sigma) (90 mg/ml) was injected intraperitoneally, daily for 5 days into 12- to 13-week-old mice as previously described (54). The mice were sacrificed 3 days after the last injection.

DSS model

DSS with average molecular weight of 36,000 to 50,000 Da (MP Biomedicals) was added for 7 days to the sterile drinking water of 7- to 10-week-old C57BL/6 (WT) male mice at a concentration of 2.5 or 4% and was administered *ad libitum*. Body weight and blood in stool were monitored daily.

Tissue collection and handling

Mice were euthanized and tissues (TI and distal colon) were collected and gently rinsed with cold PBS solution. Samples were either fixed in 4% paraformaldehyde (Bar Naor) for histological experiments or quickly frozen in liquid nitrogen and then stored at −80 °C for RNA and protein extraction.

Tissue fixation, immunohistochemistry, and immunofluorescence staining

Mouse tissues were fixed in 4% paraformaldehyde solution for at least 16 h and then dehydrated with 70% ethanol. Tissues were subsequently embedded in paraffin by the Rambam Medical Center Pathology Unit. Blocks were then sectioned (5-μm thick) using a Shandon Finesse 325 Manual Rotary Microtome (Thermo Fisher Scientific). Sections were fixed onto Superfrost microscope slides and later deparaffinized with xylene and rehydrated in a series of graded ethanol. For the DSS experiments, tissues were handled similarly and then cut to 3-μm thick sections.

Mouse tissue histology

H&E staining

For H&E staining, paraffin-embedded TI sections were deparaffinized with xylene and rehydrated in 100% ethanol and then in 95% ethanol. Staining was performed with Harris hematoxylin solution (Sigma) and eosin Y (Sigma), as per the manufacturer's instructions.

Perls' Prussian blue iron staining

Paraffin-embedded TI sections, prepared as described, were incubated with freshly prepared Perls' Prussian blue solution (2% hydrochloric acid mixed with 2% potassium ferrocyanide) to reveal iron content and distribution. Quantification was evaluated by morphometric means as described previously (55).

Assessment of IBD

H&E-stained sections were graded (0: no change; 1: minimal; 2: mild; 3: moderate; 4: severe) by a blinded board-certified pathologist, based on standard histologic criteria (56).

Mouse tissue IF

Mice with genetic modifications

Paraffin-embedded TI sections, prepared as described above for the iron stain, underwent antigen retrieval by incubation in citrate buffer (1×) in a microwave for approximately 10 min until boiling was observed. Following this, the sections were thoroughly rinsed with distilled water and blocked with 10% normal goat serum (Jackson) in PBS containing 0.1% bovine serum albumin (BSA, Sigma). For immunofluorescent staining, the sections were incubated overnight at room temperature (RT) in a humidified chamber with an affinity-purified rabbit anti-mouse liver ferritin antibody (1:200 dilution), kindly provided by Prof. A. M. Konijn. Afterward, the slides were washed three times with 1 × PBS. To detect the primary antibody, Alexa Fluor 488–conjugated anti-rabbit secondary antibodies (A11034, Invitrogen) were used at a dilution of 1:1000 in PBS containing 0.1% BSA. The secondary antibodies were incubated with the sections for 1 h at RT. Following the

incubation, the slides were washed three times with 1 × PBS for 5 min. The stained sections were mounted with VECTASHIELD mounting medium containing 4′,6-diamidino-2-phenylindole (VE-H-1200, Vector laboratories) to visualize the nuclei. Negative controls were included, where sections were incubated only with secondary antibodies. Microscopic imaging and fluorescent visualization were conducted using a Nikon Eclipse 50i microscope equipped with an X-cite series 120 microscope light source system. The acquisition software used for imaging was NIS-Elements Microscope Imaging Software (https://www.microscope.healthcare.nikon.com/en_EU/products/software/nis-elements). The fluorescent signal was quantified using IMARIS software (https://imaris.oxinst.com).

DSS model

IF staining of ferritin in DSS treated mice and their controls, tissue sections (3-μm thick) were utilized. The tissue sections were incubated overnight at 4 °C with a rabbit anti-FtH antibody, which was in-house produced at Kuanyu Li's lab, Nanjing University Medical School. The primary antibody was diluted 1:1000 in PBS containing 1% BSA. Following the incubation with the primary antibody, the slides were incubated with Alexa Fluor 488 AffiniPure Goat Anti-Rabbit IgG (Jackson ImmunoResearch Laboratories) secondary antibody at a dilution of 1:1000 in PBS containing 1% BSA. For nuclear counterstaining, 4′,6-diamidino-2-phenylindole (Servicebio) was used. After the staining process, slides were drained and mounted using AntiFade Mounting Medium (Servicebio) to preserve the fluorescence and prevent photobleaching. The stained tissue sections were visualized under a confocal microscope.

Fractionation of TI to EC-enriched and immune cell–enriched fractions

Fractionation was done according to a well-established protocol (57) with minor changes. Mice were sacrificed and the TI was carefully dissected, opened, and rinsed with cold deoxygenated PBS. To isolate ECs, the tissue was cut into segments and immersed in 1× Hank's Balanced Salt Solution supplemented with 20% fetal bovine serum (FBS), 1 mM DTT, and 2 mM ethylenediaminetetraacetic acid. The segments were then incubated at 37 °C for 30 min with shaking to facilitate cell dissociation. The resulting solution was passed through a fine mesh filter to remove debris, and the suspended cells were pelleted by centrifugation at 212*g*. The cells were subsequently washed twice with PBS. For the isolation of immune cells, the remaining tissue was immersed in PBS containing 0.492 mM $CaCl_2$ and 0.9 mM $MgCl_2$, supplemented with 20% FBS, collagenase (1 mg/ml, C0130, Sigma), and DNase (0.1 mg/ml, 4716728001, Sigma). Similar to the EC isolation, the segments were incubated at 37 °C for 30 min with shaking. The resulting solution was then passed through a fine mesh filter, and the suspended immune cells were pelleted by centrifugation at 212*g* and washed twice with PBS. Both the isolated epithelial and immune cells were snap-frozen in liquid nitrogen and stored at −80 °C until further use. Tissue fractionation was carried out in an anaerobic environment to ensure the preservation of cellular integrity and oxygen-sensitive molecules. Notably, all solutions used for the isolation procedures were thoroughly degassed to minimize exposure to oxygen during cell isolation and maintain an anaerobic environment.

Cultivation of cell lines

Caco2 cells (American Type Culture Collection CR2 2101) and Raw 264.7 cells (a kind gift of Prof. B. Levi, Technion) were cultured in Dulbecco's modified Eagle medium (DMEM, Sigma) supplemented with 10% heat-inactivated fetal calf serum (FCS) (Biological Industries), 1% L-glutamine (Biological Industries), and 1% Pen-Strep (Biological Industries), at 37 °C in 5% CO_2. Periodic testing for mycoplasma contamination was conducted on both cell lines to ensure data reliability.

Primary cultures of BMDMs

Femurs and tibias were harvested from C57BL/6 mice (WT and *Irp1*$^{-/-}$). Bone marrow cells were obtained by thorough flushing of the bones with DMEM. Following red blood cell lysis, cells were plated in DMEM supplemented with 20% FCS, 30% CCL1 cell–conditioned medium (CCL1 cells were a kind gift of Dr J. Kaplan, University of Utah), 1% L-glutamine, and 1% Pen-Strep (all from Biological Industries). The cells were cultured for 6 days in petri dishes.

On day 6, fully differentiated macrophages were scraped from the petri dishes on ice. The cells were then replated in PBS for 30 min. Subsequently, the PBS was replaced with DMEM containing 10% FCS, 1% Pen-Strep, and 1% glutamine for further experimentation.

Interspecies coculture assembly

The day before coculture assembly, Caco2 cells were grown in an oxygen-modified incubator (6% O_2). Confluent cocultures of ECs and macrophages were obtained by seeding 2 × 10^5 cells per cm^2 surface area. For Caco2-Raw 264.7 cocultures, Raw 264.7 cells were seeded and then Caco2 cells were added to them after 24 h. For Caco2-BMDM cocultures, on day 6 after bone marrow extraction, the cells were plated as described above, and Caco2 cells were added to them after 24 h. Cocultures were cultivated in an oxygen-modified incubator (6% O_2), at 37 °C and 5% CO_2. Treatments of ferric ammonium citrate (ammonium iron (III) citrate, F5879, Sigma), desferrioxamine (deferoxamine mesylate salt, D9533, Sigma), LPS (from *Escherichia coli* O111:B4, L4391, Sigma) and Tempol (4-hydroxy-TEMPO (TEMPOL), 176141, Sigma) were carried out as detailed in the Figure legends.

Cell lysate preparation

After the specified treatments, cells were lysed in degassed lysis buffer comprised of 10 mM Hepes (pH 7.2), 3 mM $MgCl_2$, 40 mM KCl, 5% glycerol, 0.2% Nonidet P-40, 5 mM DTT, 1 mM 4-(2-Aminoethyl) benzenesulfonyl fluoride hydrochloride (AEBSF), 10 g/ml leupeptin and Complete EDTA-free

protease inhibitor cocktail (11836170001, Roche). The lysis process was carried out for 10 min on ice. Nuclei and cellular debris were removed by centrifugation at 4 °C for 15 min at 14,500*g*. Cell lysates were prepared in an anaerobic chamber to maintain oxygen-free environment. The protein concentrations in the cell lysate were determined using the Bradford assay.

Western blotting and antibodies

Equal amounts of protein (40 μg/lane) were separated by SDS-PAGE and transferred onto nitrocellulose or polyvivylidene fluoride membranes. The transferred membranes were blocked with a blocking solution and probed with primary antibodies at 4 °C, as detailed in Table S1. Secondary horse-radish peroxidase-conjugated IgG antibodies used are listed in Table S3. Blots were developed using enhanced chemiluminescence (ECL kit, Pierce) to visualize the proteins bands on the membranes.

RNA mobility shift assays

Gel retardation assays were performed following the previously described method (14). Cell lysates were prepared as described above-mentioned section. Five micrograms total protein were added to a final volume of 12.5 μl buffer containing 25 mM Tris–HCl (pH 7.5) and 40 mM KCl, with or without 2% 2-mercaptoethanol, which activates IRP1 *in vitro*. The protein samples were incubated for 5 min at RT with 12.5 μl reaction cocktail containing 20% glycerol, 0.2 U/μl Super RNAsine (Ambion), 0.6 μg/μl yeast tRNA (J61215, Thermo Fisher Scientific), 5 mM DTT, and 20 nM ^{32}P-labeled (NEG508H250UC, PerkinElmer) IRE from the human ferritin H chain gene. The reaction was conducted in 25 mM Tris–HCl (pH 7.5), and 40 mM KCl. After the incubation, samples (20 μl) of the reaction were loaded onto a 10% acrylamide/Tris-borate-ethylenediaminetetraacetic acid gel. The gel was run at 200 V for 2.25 h. Following electrophoresis, the gel was then fixed, dried, and exposed for autoradiography.

Aconitase assays

Mitochondrial and cytosolic aconitase activities in cell lysates were assayed concurrently after electrophoretic separation, as previously described (58). Protein concentrations in the cell lysate were quantified using the Bradford assay. Then 400 μg of protein were loaded into 8% polyacrylamide/Tris-borate-ethylenediaminetetraacetic acid gel supplemented with 1 M Na citrate and run at 180 V for 5 h in running buffer [25 mM tris base, 192 mM glycine, and 3.6 mM citrate (pH 8)]. Gel was washed with distilled water and incubated at 37 °C for 5 to 45 min in reaction solution [100 mM tris (pH 8.0), 1 mM nicotinamide adenine dinucleotide phosphate, 2.5 mM cis-aconitate, 5 mM $MgCl_2$, 1.2 mM 3-(4,5-dimethylthiazol-2-yl)-2,5-diphenyltetrazolium bromide, 0.3 mM phenazine methosulfate, and isocitrate dehydrogenase (5 U/ml)]. All chemicals were purchased from Sigma. Gel is washed three times with distilled water for 5 min to remove background and gel is imaged.

Quantitative RT-PCR

Total RNA was extracted using the Trizol reagent (Invitrogen). For cell samples, cells were harvested directly with Trizol, while for tissue samples, tissues were first ground in liquid N_2-cooled mortars and then incubated with Trizol, in accordance with the manufacturer's instructions. Isolated RNA samples were subjected to DNase treatment using the DNase I recombinant, RNase-free kit (Quanta biosciences). Complementary DNA was synthesized using the complementary DNA Reverse Transcription Kit (Quanta biosciences). Quantitative RT-PCRs were performed using the SYBR master mix (Applied Biosystems). All primers used in the study are listed in Table S5. The relative expression of the target genes was calculated using the delta Ct method, normalizing to the expression of topoisomerase 1 for ECs and ubiquitin for macrophage genes.

Subcellular fractionation

Cells were first suspended in lysis buffer comprised of 10 mM Hepes (pH 7.9), 10 mM KCl, 1.5 mM $MgCl_2$, 0.34 M sucrose, 10% glycerol, 1 mM DTT, 1 mM AEBSF, and Complete TM EDTA-free protease inhibitor cocktail. Triton 0.1% was then added to the cell suspension and incubated for 5 min. The cell suspension was then centrifuged at 1500*g* for 4 min. The supernatant was carefully transferred to a new tube and was considered the crude cytoplasm-enriched fraction. The pellet obtained from previous step was then washed with the first lysis buffer then lysed in a second lysis buffer comprised of 3 mM EDTA, 0.2 mM EGTA, 1 mM DTT, 1 mM AEBSF, and Complete TM EDTA-free protease inhibitor cocktail. The lysate was incubated for 10 min and then centrifuged at 1700*g* for 4 min. The supernatant was transferred to a new tube and was considered the nucleoplasmic fraction. The pellet obtained from previous step was then first washed in the second lysis buffer then suspended in the first lysis buffer supplemented with 1 mM $CaCl_2$ and 0.6 U of MNase (NEB-M0247S, New England Biologicals). The sample was incubated for 30 min at 37 °C. After centrifuging the sample at 20,000*g* for 10 min, the supernatant was transferred to a new tube and was considered the chromatin-bound fraction. The crude cytosol-enriched fraction was further centrifuged at 20,000*g* for 10 min; the supernatant was transferred to a new tube and was considered the cytosol-enriched fraction. All steps were performed in an anaerobic environment, and all lysis buffers were degassed.

Labeling cells with ^{55}Fe

To detect iron inside the cells and in media, cells were given medium containing transferrin loaded with labeled iron. To prepare this labeled transferrin, 200 mM of nitrilotriacetic acid (NTA) was dissolved in 0.9% NaCl and equilibrated to pH 3 with NaOH (10N). Then, 100 mM cold $FeCl_3$ (Fe^{56}) was dissolved in 0.1 M HCl. Hot-Fe$(NTA)_2$ was prepared in a volume ratio of 4:1:5 by mixing cold $FeCl_3$, hot $^{55}FeCl_3$ (^{55}Fe NEZ-043-001MC, PerkinElmer), and NTA, respectively. The mixture was incubated for 30 min at RT.

Subsequently, to allow for iron loading, apotransferrin (T1428, Sigma, in Hank's Balanced Salt Solution) was mixed

with hot-$^{55}Fe(NTA)_2$ at a molar ratio of 1:4, comprising 125 μl of 1 mM apotransferrin, 12.5 μl of 0.5 M $NaHCO_3$, and 10 μl of 50 mM hot $^{55}Fe(NTA)_2$. Following a short incubation, which yielded a pink solution, 2 ml of medium was introduced. The resultant mixture was then filtered and added to the cells. After overnight incubation, the medium was removed and cells were washed twice with PBS. To induce inflammation in the ^{55}Fe labeled cocultures, LPS (200 ng/ml) was added for the indicated time intervals. Harvested cells were snap-frozen and stored at −80 °C until further use.

Metabolic labeling and immunoprecipitation

Cells were metabolically labeled for 1 h with ^{35}S Translabel (NEG772007MC, PerkinElmer, mCi per 5 ml DMEM) without cysteine and methionine. The medium was supplemented with 10% dialyzed FCS, 10 mM Hepes, 1% pen/strep, and 1% glutamine. After metabolic labeling, cells were lysed in lysis buffer comprised of 1% Triton X-100, 20 mM Tris (pH 8.0), 37 mM NaCl, 10% glycerol, and EDTA-free protease inhibitor cocktail. Lysates were first precleared with noncoated protein A-sepharose beads (L00210, GeneScript). The supernatants from the precleared samples were then transferred to fresh tubes containing slurry of protein A-sepharose beads coated with anti-FtH antibodies (GE-Healthcare). The samples were rotated for 3 h at 4 °C and then centrifuged at 800*g* to isolate the immunoprecipitated proteins. The immunoprecipitated proteins were denatured with reducing 1× sample buffer and boiled at 95 °C for 5 min. Subsequently, samples were then resolved by 14% SDS-PAGE. The SDS-PAGE gel was fixed, dried, and exposed for autoradiography to visualize the labeled proteins.

SNAP treatment

The day before SNAP treatment, Caco2 cells were cultured in minimum essential medium (Sigma) supplemented with 20% heat-inactivated FCS, 20 μM ferric ammonium citrate, 1 mM nonessential amino acids (Gibco), 10 mM sodium pyruvate (Gibco), 2 mM L-glutamine, and 1% Pen-strep. The cells were cultured in an oxygen-controlled incubator (6% O_2) at 37 °C with 5% CO_2.

SNAP (N3398, Sigma) was added to the cells for 22 h and administered in two sequential doses. The first dose of SNAP was added to the cells and they were incubated for 6 h. After the initial 6-h incubation, 20% of the medium was collected from the culture and replaced with medium containing 5 mM SNAP. The cells were then further incubated for an additional 15 h.

SNAP treatment in ^{55}Fe-labeled Caco2 cells

Caco2 cells were treated with SNAP following the same protocol as described above. After the overnight SNAP incubation, cells were harvested at each designated time point. Subsequently, the cells were snap-frozen and stored at −80 °C for further analysis.

Griess assays

Nitrite concentration in the medium was determined using the Griess assay. Briefly, the medium was collected and centrifuged at 1000*g*. Supernatant (50 μl) was then added to 50 μl of 1% sulfanilamide in 5% phosphoric acid. The mixture was incubated in the dark for 10 min. Next, 50 μl of 0.1 N-1-naphthylethylenediamine dihydrochloride was added. The reaction product was measured with the spectrocolorimeter (Multiskan EX, Thermo Electron Corporation), at 540 nm. $NaNO_2$ was used to create a standard curve of nitrite.

Ferritin transfection

HEK293T cells were grown in DMEM supplemented with 10% heat-inactivated FBS, 2 mM L-glutamine and 1% penicillin-streptomycin. The indicated ferritin constructs were transfected with polyethylenimine, according to standard protocol. Cells were harvested ∼40 h posttransfection for subsequent analysis.

Native-PAGE stains

Samples were heat treated for 10 min in 70 °C and precipitated before separation on 6% Native-PAGE to visualize ferritin complexes.

Perls'-DAB iron stain

Gel is rinsed and then incubated for 1 h at RT with Perls' Prussian blue staining solutions (4% potassium ferrocyanide and 1.3% (v/v) HCl, mixed right before incubation). Gel is rinsed until neutral pH achieved and incubated in 100 mM Tris buffer (pH 7), for 5 min. The stain is then enhanced by incubation with 3,3′-diaminutesobenzidine (328005000, Thermo Fisher Scientific) solution (1% dimethylsulfoxide, 0.05% H_2O_2, 0.025% 3,3′-diaminutesobenzidine in 100 mM Tris buffer, pH 7) for 2 h for initial signal and overnight for saturation.

Coomassie stain

After electrophoresis, native gels were gently washed in the tap water and placed directly into staining solution InstantBlue Coomassie Protein Stain (Ab119211, Abcam), according to the manufacturers' protocol.

Human TI tissues

Human biopsies were obtained from patients with clinically active CD who were undergoing routine endoscopy or colonoscopy as part of their standard medical care. CD diagnosis was based on standard clinical, radiological, endoscopic, and histologic criteria. Biopsies were collected from both, inflamed and normal-appearing mucosa segments of each patient. The study protocol was approved by the institutional committee (IRB number 0052-17-RMB) abed by declaration of Helsinki principles and each patient provided informed consent before participating in the study. Inflammation in the biopsied tissues was determined based on the endoscopic appearance of the mucosa. Inflammation was characterized (among others) by ulceration, erosion, lack of vascularity, edema, and erythema. Paraffin-embedded blocks of the human TI segments used for this study were provided by the Rambam Medical Center histology unit. Immunofluorescent staining of ferritin was

performed following the same protocol as described for mouse samples.

Statistical analysis

Statistical analysis was performed using Graph Pad Prism 8 (GraphPad Software, http://app.graphpad.com/). Values in graphs are expressed as mean ± SD (unless otherwise specified). Data were examined for normality of distribution and variance homogeneity. Two groups of mice were compared with Student's two-tailed t test for independent data. $p < 0.05$ ($^{*}p < 0.05$, $^{**}p < 0.01$, $^{***}p < 0.001$, and $^{****}p < 0.0001$) was considered significant.

Data availability

All materials are available from the authors on reasonable request with materials transfer agreements.

Supporting information—This article contains Supporting information.

Acknowledgments—We like to thank Dr T.A. Rouault (NICHD, NIH) for providing the IRP1$^{-/-}$ mice, Dr F. Cominelli (Case Western Reserve University) for initially providing the *Tnf* $^{\Delta ARE/+}$ mice, and Dr G. Kollias (BSRC Alexander Fleming Athens University Medical School) for subsequently sharing with us the *Tnf* $^{\Delta ARE/+}$ mice; Dr Orly Savion and Dr Aileen Harrer for technical assistance; Drs Dan Gelvan, Vasiliki Koliaraki, Benjamin Podbilewicz, and Dan Cassel and many former and present lab members of the E. G. M.-H. lab for critically reviewing the manuscript and supporting this project with the thoughts and discussions.

Author contributions—L. F. data curation; L. F., S. M.-B., K. Z., N. G., N. G.-R., W. Z., K. L., W.-H. T., A. N., M. W., R. W., and A. Z. investigation; L. F., S. M.-B., K. Z., N. G., N. G.-R., W. Z., A. N., M. W., R. W., and A. Z. methodology; L. F., S. M.-B., and E. G. M.-H. project administration; L. F., S. M.-B., K. Z., W. Z., and A. Z. visualization; L. F., S. M.-B., W.-H. T., and E. G. M.-H. writing–original draft; L. F., K. Z., N. G., N. G.-R., K. L., W.-H. T., and E. G. M.-H. writing–review and editing; N. G.-R. and E. G. M.-H. funding acquisition; E. G. M.-H. conceptualization; E. G. M.-H. supervision.

Funding and additional information—This study was supported by grants from the Israel Science Foundation (No.755/09), the Joint Canada-Israel Program of the Israel Science Foundation (No. 3549/19), the Israeli Ministry of Health (No. 2026203 and 3-15072), and the Israeli Ministry of Science and Technology (No. 3-13438) [to E. G. M.-H.].

Conflict of interest—E. G. M.-H. and L. F. are inventors on a Provisional Patent Application, "Model for Analyzing inflammation and uses," US Provisional Patent Application No. 633/38,64 related to this work filed jointly by the Technion on July 13, 2022. The other authors declare that they have no conflicts of interest with the contents of this article.

Abbreviations—The abbreviations used are: BAEBSF, 4-(2-aminoethyl) benzenesulfonyl fluoride hydrochloride; BMDM, bone marrow–derived macrophage; BSA, bovine serum albumin; cAco, cytosolic aconitase; CD, Crohn's disease; DMEM, Dulbecco's modified Eagle medium; DSS, dextran sulphate sodium; EC, epithelial cell; FBS, fetal bovine serum; FCS, fetal calf serum; HIF, hypoxia inducible factor; IBD, inflammatory bowel disease; IEC, intestinal epithelial cell; IF, immunofluorescent stain; IRE, iron-responsive element; IRP, iron regulatory protein; LP, lamina propria; LPS, lipopolysaccharide; NO, nitric oxide; NTA, nitrilotriacetic acid; RT, room temperature; SNAP, S-nitro-N-acetyl-D, L-penicillamine; TFR1, transferrin receptor 1; TI, terminal ileum.

References

1. Kaplan, G. G., and Windsor, J. W. (2021) The four epidemiological stages in the global evolution of inflammatory bowel disease. *Nat. Rev. Gastroenterol. Hepatol.* **18**, 56–66
2. Lih-Brody, L., Powell, S. R., Collier, K. P., Reddy, G. M., Cerchia, R., Kahn, E., *et al.* (1996) Increased oxidative stress and decreased antioxidant defenses in mucosa of inflammatory bowel disease. *Dig. Dis. Sci.* **41**, 2078–2086
3. Yu, Y., and Richardson, D. R. (2011) Cellular iron depletion stimulates the JNK and p38 MAPK signaling transduction pathways, dissociation of ASK1-thioredoxin, and activation of ASK1. *J. Biol. Chem.* **286**, 15413–15427
4. Steinbicker, A. U., and Muckenthaler, M. U. (2013) Out of balance–systemic iron homeostasis in iron-related disorders. *Nutrients* **5**, 3034–3061
5. Kroner, A., Greenhalgh, A. D., Zarruk, J. G., Passos Dos Santos, R., Gaestel, M., and David, S. (2014) TNF and increased intracellular iron alter macrophage polarization to a detrimental M1 phenotype in the injured spinal cord. *Neuron* **83**, 1098–1116
6. Ganz, T., and Nemeth, E. (2012) Hepcidin and iron homeostasis. *Biochim. Biophys. Acta* **1823**, 1434–1443
7. Wilkinson, N., and Pantopoulos, K. (2014) The IRP/IRE system in vivo: insights from mouse models. *Front Pharmacol.* **5**, 176
8. Aschemeyer, S., Qiao, B., Stefanova, D., Valore, E. V., Sek, A. C., Ruwe, T. A., *et al.* (2018) Structure-function analysis of ferroportin defines the binding site and an alternative mechanism of action of hepcidin. *Blood* **131**, 899–910
9. Nemeth, E., Tuttle, M. S., Powelson, J., Vaughn, M. B., Donovan, A., Ward, D. M., *et al.* (2004) Hepcidin regulates cellular iron efflux by binding to ferroportin and inducing its internalization. *Science* **306**, 2090–2093
10. Harford, J. B., and Klausner, R. D. (1990) Coordinate post-transcriptional regulation of ferritin and transferrin receptor expression: the role of regulated RNA-protein interaction. *Enzyme* **44**, 28–41
11. Hanson, E. S., and Leibold, E. A. (1999) Regulation of the iron regulatory proteins by reactive nitrogen and oxygen species. *Gene Expr.* **7**, 367–376
12. Meyron-Holtz, E. G., Ghosh, M. C., and Rouault, T. A. (2004) Mammalian tissue oxygen levels modulate iron-regulatory protein activities in vivo. *Science* **306**, 2087–2090
13. Kühn, L. C. (2015) Iron regulatory proteins and their role in controlling iron metabolism. *Metallomics.* **7**, 232–243
14. Meyron-Holtz, E. G., Ghosh, M. C., Iwai, K., LaVaute, T., Brazzolotto, X., Berger, U. V., *et al.* (2004) Genetic ablations of iron regulatory proteins 1 and 2 reveal why iron regulatory protein 2 dominates iron homeostasis. *EMBO J.* **23**, 386–395
15. Schneider, B. D., and Leibold, E. A. (2003) Effects of iron regulatory protein regulation on iron homeostasis during hypoxia. *Blood* **102**, 3404–3411
16. Cross, R. K., and Wilson, K. T. (2003) Nitric oxide in inflammatory bowel disease. *Inflamm. Bowel Dis.* **9**, 179–189
17. Recalcati, S., Gammella, E., and Cairo, G. (2019) Ironing out macrophage immunometabolism. *Pharmaceuticals* **12**, 94
18. Kontoyiannis, D., Pasparakis, M., Pizarro, T. T., Cominelli, F., and Kollias, G. (1999) Impaired on/off regulation of TNF biosynthesis in mice lacking TNF AU-rich elements: implications for joint and gut-associated immunopathologies. *Immunity* **10**, 387–398
19. Solomon, L., Mansor, S., Mallon, P., Donnelly, E., Hoper, M., Loughrey, M., *et al.* (2010) The dextran sulphate sodium (DSS) model of colitis: an overview. *Comp. Clin. Path* **19**, 235–239

20. Harrison, P. M., and Arosio, P. (1996) The ferritins: molecular properties, iron storage function and cellular regulation. *Biochim. Biophys. Acta* **1275**, 161–203
21. Hartwig, O., Shetab Boushehri, M. A., Shalaby, K. S., Loretz, B., Lamprecht, A., and Lehr, C. M. (2021) Drug delivery to the inflamed intestinal mucosa – targeting technologies and human cell culture models for better therapies of IBD. *Adv. Drug Deliv. Rev.* **175**, 113828
22. Tanoue, T., Nishitani, Y., Kanazawa, K., Hashimoto, T., and Mizuno, M. (2008) In vitro model to estimate gut inflammation using co-cultured Caco-2 and RAW264.7 cells. *Biochem. Biophys. Res. Commun.* **374**, 565–569
23. Chen, L., Deng, H., Cui, H., Fang, J., Zuo, Z., Deng, J., *et al.* (2017) Inflammatory responses and inflammation-associated diseases in organs. *Oncotarget* **9**, 7204–7218
24. Liu, T., Zhang, L., Joo, D., and Sun, S. C. (2017) NF-κB signaling in inflammation. *Signal. Transduct. Target Ther.* **2**, 17023
25. Lund, S., Christensen, K. V., Hedtjärn, M., Mortensen, A. L., Hagberg, H., Falsig, J., *et al.* (2006) The dynamics of the LPS triggered inflammatory response of murine microglia under different culture and in vivo conditions. *J. Neuroimmunol.* **180**, 71–87
26. Bouton, C., Chauveau, M. J., Lazereg, S., and Drapier, J. C. (2002) Recycling of RNA binding iron regulatory protein 1 into an aconitase after nitric oxide removal depends on mitochondrial ATP. *J. Biol. Chem.* **277**, 31220–31227
27. Tannahill, G. M., Curtis, A. M., Adamik, J., Palsson-McDermott, E. M., McGettrick, A. F., Goel, G., *et al.* (2013) Succinate is an inflammatory signal that induces IL-1β through HIF-1α. *Nature* **496**, 238–242
28. Canal, F., Fosset, C., Chauveau, M. J., Drapier, J. C., and Bouton, C. (2007) Regulation of the cysteine desulfurase Nfs1 and the scaffold protein IscU in macrophages stimulated with interferon-gamma and lipopolysaccharide. *Arch. Biochem. Biophys.* **465**, 282–292
29. Giatromanolaki, A., Sivridis, E., Maltezos, E., Papazoglou, D., Simopoulos, C., Gatter, K. C., *et al.* (2003) Hypoxia inducible factor 1alpha and 2alpha overexpression in inflammatory bowel disease. *J. Clin. Pathol.* **56**, 209–213
30. Mastrogiannaki, M., Matak, P., and Peyssonnaux, C. (2013) The gut in iron homeostasis: role of HIF-2 under normal and pathological conditions. *Blood* **122**, 885–892
31. Recalcati, S., Taramelli, D., Conte, D., and Cairo, G. (1998) Nitric oxide-mediated induction of ferritin synthesis in J774 macrophages by inflammatory cytokines: role of selective iron regulatory protein-2 down-regulation. *Blood* **91**, 1059–1066
32. Ruscitti, P., Di Benedetto, P., Berardicurti, O., Panzera, N., Grazia, N., Lizzi, A. R., *et al.* (2020) Pro-inflammatory properties of H-ferritin on human macrophages, ex vivo and in vitro observations. *Sci. Rep.* **10**, 12232
33. Roulis, M., Armaka, M., Manoloukos, M., Apostolaki, M., and Kollias, G. (2011) Intestinal epithelial cells as producers but not targets of chronic TNF suffice to cause murine Crohn-like pathology. *Proc Natl Acad Sci U. S. A.* **108**, 5396–5401
34. Choi, E. Y., Kim, E. C., Oh, H. M., Kim, S., Lee, H. J., Cho, E. Y., *et al.* (2004) Iron chelator triggers inflammatory signals in human intestinal epithelial cells: involvement of p38 and extracellular signal-regulated kinase signaling pathways. *J. Immunol.* **172**, 7069–7077
35. Ghosh, M. C., Tong, W. H., Zhang, D., Ollivierre-Wilson, H., Singh, A., Krishna, M. C., *et al.* (2008) Tempol-mediated activation of latent iron regulatory protein activity prevents symptoms of neurodegenerative disease in IRP2 knockout mice. *Proc Natl Acad Sci U. S. A.* **105**, 12028–12033
36. Chang, J. T. (2020) Pathophysiology of inflammatory bowel diseases. *N. Engl. J. Med.* **383**, 2652–2664
37. Medzhitov, R. (2021) The spectrum of inflammatory responses. *Science* **374**, 1070–1075
38. Meli, R., Mattace Raso, G., Irace, C., Simeoli, R., Di Pascale, A., Paciello, O., *et al.* (2013) High fat diet induces liver steatosis and early dysregulation of iron metabolism in rats. *PLoS One* **8**, e66570
39. Tong, W. H., Maio, N., Zhang, D. L., Palmieri, E. M., Ollivierre, H., Ghosh, M. C., *et al.* (2018) TLR-activated repression of Fe-S cluster biogenesis drives a metabolic shift and alters histone and tubulin acetylation. *Blood Adv.* **2**, 1146–1156
40. Saito, T., Fukai, A., Mabuchi, A., Ikeda, T., Yano, F., Ohba, S., *et al.* (2010) Transcriptional regulation of endochondral ossification by HIF-2alpha during skeletal growth and osteoarthritis development. *Nat Med* **16**, 678–686
41. Richardson, D. R., and Lok, H. C. (2008) The nitric oxide-iron interplay in mammalian cells: transport and storage of dinitrosyl iron complexes. *Biochim. Biophys. Acta* **1780**, 638–651
42. Shah, Y. M., Matsubara, T., Ito, S., Yim, S. H., and Gonzalez, F. J. (2009) Intestinal hypoxia-inducible transcription factors are essential for iron absorption following iron deficiency. *Cell Metab.* **8**, 3252–3264
43. Ghatpande, N., Harrer, A., Azoulay-Botzer, B., Guttmann-Raviv, N., Bhushan, S., Meinhardt, A., *et al.* (2024) Iron regulatory proteins 1 and 2 have opposing roles in regulating inflammation in bacterial orchitis. *JCI Insight* **9**, e175845
44. Werner, T., Hoermannsperger, G., Schuemann, K., Hoelzlwimmer, G., Tsuji, S., and Haller, D. (2009) Intestinal epithelial cell proteome from wild-type and TNFDeltaARE/WT mice: effect of iron on the development of chronic ileitis. *J. Proteome Res.* **8**, 3252–3264
45. Das, N. K., Schwartz, A. J., Barthel, G., Inohara, N., Liu, Q., Sankar, A., *et al.* (2020) Microbial metabolite signaling is required for systemic iron homeostasis. *Cell Metab.* **31**, 115–130.e6
46. Bessman, N. J., Mathieu, J. R. R., Renassia, C., Zhou, L., Fung, T. C., Fernandez, K. C., *et al.* (2020) Dendritic cell-derived hepcidin sequesters iron from the microbiota to promote mucosal healing. *Science* **368**, 186–189
47. Bruckner, R. S., Nissim-Eliraz, E., Marsiano, N., Nir, E., Shemesh, H., Leutenegger, M., *et al.* (2019) Transplantation of human intestine into the mouse: a novel platform for study of inflammatory enterocutaneous fistulas. *J. Crohns Colitis* **13**, 798–806
48. Mancias, J. D., Wang, X., Gygi, S. P., Harper, J. W., and Kimmelman, A. C. (2014) Quantitative proteomics identifies NCOA4 as the cargo receptor mediating ferritinophagy. *Nature* **509**, 105–109
49. Kuno, S., Fujita, H., Tanaka, Y. K., Ogra, Y., and Iwai, K. (2022) Iron-induced NCOA4 condensation regulates ferritin fate and iron homeostasis. *EMBO Rep.* **23**, 1–18
50. Ohshima, T., Yamamoto, H., Sakamaki, Y., Saito, C., and Mizushima, N. (2022) NCOA4 drives ferritin phase separation to facilitate macroferritinophagy and microferritinophagy. *J. Cell Biol.* **221**, 1–14
51. Wilkinson, N., and Pantopoulos, K. (2013) IRP1 regulates erythropoiesis and systemic iron homeostasis by controlling HIF2alpha mRNA translation. *Blood* **122**, 1658–1668
52. Ghosh, M. C., Zhang, D. L., Jeong, S. Y., Kovtunovych, G., Ollivierre-Wilson, H., Noguchi, A., *et al.* (2013) Deletion of iron regulatory protein 1 causes polycythemia and pulmonary hypertension in mice through translational derepression of HIF2alpha. *Cell Metab.* **17**, 271–281
53. Starzynski, R. R., Lipinski, P., Drapier, J. C., Diet, A., Smuda, E., Bartlomiejczyk, T., *et al.* (2005) Down-regulation of iron regulatory protein 1 activities and expression in superoxide dismutase 1 knock-out mice is not associated with alterations in iron metabolism. *J. Biol. Chem.* **280**, 4207–4212
54. Weiss, A., Spektor, L., Cohen, L. A., Lifshitz, L., Gold, I. M., Zhang, D.-L., *et al.* (2018) Orchestrated regulation of iron trafficking proteins in the kidney during iron overload facilitates systemic iron retention. *PLoS One* **13**, 1–16
55. Nyska, A., Waner, T., Scolnik, M., Zuckerman, A., Pirak, M., Kuehnberg, W., *et al.* (1989) Quantitative evaluation of chlortoluran-induced splenic hemosiderosis by means of an image analyzer. *Vet. Hum. Toxicol.* **31**, 218–221
56. Schafer, K. A., Eighmy, J., Fikes, J. D., Halpern, W. G., Hukkanen, R. R., Long, G. G., *et al.* (2018) Use of severity grades to characterize histopathologic changes. *Toxicol. Pathol.* **46**, 256–265
57. Smillie, C. S., Biton, M., Ordovas-Montanes, J., Sullivan, K. M., Burgin, G., Graham, D. B., *et al.* (2019) Intra- and inter-cellular rewiring of the human colon during ulcerative colitis. *Cell* **178**, 714–730.e22
58. Tong, W. H., and Rouault, T. A. (2006) Functions of mitochondrial ISCU and cytosolic ISCU in mammalian iron-sulfur cluster biogenesis and iron homeostasis. *Cell Metab.* **3**, 199–210